applied sciences

MDPI

Article

Experimental Study on Macroscopic and Microscopic Tensile Strength Characteristics of Steel-Fiber-Reinforced Rubber Concrete

Ao Liu [1], Naizhong Xu [1,*], Chang Su [2] and Yu Zhang [1]

[1] School of Mining Engineering, Anhui University of Science and Technology, Huainan 232001, China; 2022304842@aust.edu.cn (A.L.); miningearth@126.com (Y.Z.)
[2] School of Mechanical Engineering, Anhui University of Science and Technology, Huainan 232001, China; suchang_user@163.com
* Correspondence: nzxu@aust.edu.cn; Tel.: +86-15-222981752

Abstract

This study examined the reported splitting-tensile response of 17 concrete mixtures labeled by nominal rubber replacement levels of 5–20% and steel fibers at 0–1.5% by volume after 7 and 28 days of curing. The reported strength values were considered together with failure photographs, representative load-displacement curves, acoustic-emission (AE) energy records for three selected mixtures, and qualitative scanning electron microscopy (SEM) observations. Rubber addition was associated with lower splitting-tensile strength, whereas several rubber–fiber mixtures recovered or exceeded the ordinary-concrete value. Among the tested combinations, SF1RR5C had the highest reported strength (4.27 MPa at 28 days, 12.4% above the ordinary-concrete value). The load-displacement curves and post-failure photographs indicate delayed separation and residual load capacity in the fiber-containing specimens. The AE and SEM observations provide qualitative, mixture-specific evidence consistent with crack bridging; they do not independently quantify internal damage, porosity, or fiber-matrix bond strength.

Keywords: concrete; rubber; steel fiber; splitting tensile strength; acoustic emission; scanning electron microscopy

1. Introduction

Concrete is widely used because of its compressive capacity, availability, and versatility, but its low tensile resistance and quasi-brittle fracture can limit performance under cracking-sensitive loading [1–5]. Waste-tire rubber has been investigated as a partial aggregate substitute because its low stiffness and high deformability can delay crack localization and increase deformation capacity. Yuan et al. [6] reviewed waste tire recycling strategies under the extended producer responsibility system, establishing the environmental motivation for rubber utilization in construction materials. Yao et al. [7] investigated the performance degradation and microstructural changes of rubber concrete after salt freeze–thaw cycles, reporting that rubber particles modify the pore structure but may compromise long-term durability under aggressive environments. Xue et al. [8] studied the uniaxial compression fatigue performance of rubber concrete, demonstrating that rubber incorporation reduces stiffness yet improves deformation capacity under cyclic loading. The energy-dissipation potential of rubber in composite systems has also been documented. Jin et al. [9] analyzed the dynamic response of rockfall impact on crushed stone–rubber

Check for updates

Received: 24 June 2026
Revised: 27 August 2026
Accepted: 3 September 2026
Published: 10 September 2026

Copyright: © 2026 by the authors. Licensee MDPI, Basel, Switzerland. This article is an open access article distributed under the terms and conditions of the Creative Commons Attribution (CC BY) license.

mixed cushions, showing that rubber–stone mixtures exhibit superior energy absorption compared to pure stone layers. Shi et al. [10] predicted the basic performance of rubber asphalt using a GA-BP neural network, providing a methodological framework for optimizing rubber content in cementitious and asphaltic binders. While these studies demonstrate the energy-dissipation capacity of rubber in macro-scale composite systems, they do not address the splitting-tensile response or the internal damage evolution of rubberized concrete with steel-fiber reinforcement. The toughening effect of rubber in cementitious materials has been reported under various loading conditions. Li et al. [11] investigated the effects of specimen size and loading strain rate on the splitting tensile strength of steel-fiber recycled concrete, providing baseline data on how material composition and test conditions interact to influence tensile response. Fadiel et al. [12] conducted a comprehensive evaluation of the mechanical properties of rubberized concrete, reporting that moderate rubber contents can improve toughness and ductility depending on particle size and distribution; however, their study did not examine the interaction between rubber and metallic fibers. He et al. [13] examined the static and dynamic splitting tensile performance of rubberized polymer-engineered cementitious composites under thermal cycling, demonstrating that rubber helps maintain mechanical stability under complex service conditions such as temperature variations. Nevertheless, He et al. focused on polymer-modified systems rather than ordinary Portland cement concrete, leaving the thermal–mechanical behavior of conventional rubberized concrete unresolved. Although these studies establish that rubber can enhance certain deformation characteristics, they primarily focus on either plain rubberized concrete or single-variable fiber systems, leaving the combined rubber–steel fiber interaction under splitting tension insufficiently characterized. The incorporation of rubber also presents notable drawbacks. Cocchiara et al. [14] investigated the influence of FRP confinement on the compressive strength of concrete with recycled rubber, finding that without external confinement, rubberized concrete exhibits significantly reduced stiffness and strength compared to ordinary concrete. Their study emphasized that strength degradation is governed by rubber particle processing techniques and replacement ratios, yet they did not propose internal reinforcement strategies to recover the lost capacity. Wen et al. [15] studied the enhanced dynamic compressive behavior of rubberized concrete with steel–glass hybrid fibers, noting that while hybrid fibers can improve dynamic performance, the static stiffness and strength reductions caused by rubber remain problematic. These studies indicate that the mechanical performance and durability of rubberized concrete are jointly governed by rubber characteristics and service environments; however, systematic strategies for internally compensating the lost static strength—particularly under tensile stress states—remain underdeveloped. Furthermore, rubber particles exhibit weak interfacial bonding with the cement matrix and a significant mismatch in elastic modulus. Luo et al. [16] examined the synergistic effects of steel fiber and rubber powder on the physico-mechanical properties of UHPC, observing that stress concentration readily occurs at rubber–matrix interfaces and disrupts the continuity of the matrix, thereby impairing homogeneity. Tarekegn et al. [17] performed three-dimensional simulations on the influence of coated rubber chips on concrete properties, confirming that the elastic modulus mismatch between rubber and cement paste generates interfacial debonding and localized stress concentrations. These investigations highlight the interfacial weaknesses inherent in rubberized concrete; however, they do not experimentally quantify how steel fibers interact with these weakened interfaces under splitting-tensile loading, nor do they establish whether fiber bridging can effectively redistribute stresses across rubber-modified matrices.

Prior studies have separately examined rubberized concrete, steel-fiber concrete, and mixtures containing both constituents. Qureshi et al. [18] showed that rubber particle size and content strongly influence strength, while waste-fiber reinforcement can partly recover

mechanical capacity. However, their study focused on waste-fiber rather than steel-fiber reinforcement, and the splitting-tensile behavior was not systematically evaluated across a complete mixture matrix. Xue et al. [19] conducted an experimental study on the fracture toughness of rubber concrete, reporting that moderate rubber contents may improve fracture resistance through crack deflection and energy absorption at rubber particles. Hu et al. [20] investigated the mechanical properties of rubber concrete with different replacement rates, finding that while low rubber contents can slightly improve deformability, increasing rubber content generally reduces splitting and compressive strength. El-Zohairy et al. [21] evaluated the performance of rubberized concrete and the effect of temperature and stainless-steel fibers, demonstrating that environmental conditions and fiber type significantly modulate the strength–deformability relationship. Collectively, these studies indicate a strength–deformability trade-off for rubberized concrete but they do not establish a consistent design framework for optimizing rubber–steel fiber combinations under standardized splitting protocols.

The incorporation of steel fibers has been proposed as a compensatory measure for rubber-induced strength loss. Dong et al. [22] investigated the workability and mechanical properties of steel-fiber rubber concrete, reporting that steel fibers can effectively improve uniaxial compressive mechanical behavior and bridge cracks in rubberized matrices. Zhao et al. [23] developed an experimental constitutive model for the complete uniaxial compression curve of steel-fiber rubber concrete, quantifying how steel fibers restrain crack propagation and compensate for strength loss and increased brittleness caused by rubber incorporation. Nevertheless, these studies primarily address compressive behavior and fresh-state workability; the splitting-tensile response and the optimal fiber volume fraction for tensile recovery remain unresolved. Peng et al. [24] studied the effect of steel fiber content on the mechanical properties of rubber concrete, observing that steel fiber incorporation enhances toughness and crack resistance. Wang et al. [25] investigated the mechanical properties of concrete under loading and unloading conditions, providing fundamental data on hysteretic energy dissipation that is relevant to understanding the cyclic stability of fiber-reinforced systems. Zhao [26] studied the mechanical and durability performance of straw ash–rubber concrete, demonstrating that supplementary cementitious materials combined with rubber can influence long-term service stability. While these studies suggest that steel fibers improve the mechanical stability and durability of rubberized concrete under cyclic loading, they do not provide a controlled comparison of different fiber volume fractions across a complete rubber replacement matrix using identical splitting-tensile protocols.

Recent investigations have explored alternative fiber types for rubberized concrete. Yan et al. [27] conducted an experimental study on the mechanical properties of recycled spiral steel-fiber-reinforced rubber concrete, reporting that recycled spiral steel fibers can significantly improve mechanical properties compared to plain rubberized concrete. Kroviakov et al. [28] compared the corrosion resistance of fiber-reinforced concrete with steel and polypropylene fibers in acidic environments, finding that steel fibers exhibit superior long-term durability under chemical attack. These studies highlight the potential of recycled and conventional steel fibers for ensuring service stability yet they do not compare multiple fiber volume fractions within a unified experimental framework or address the specific splitting-tensile failure mechanisms of rubberized matrices with varying rubber contents.

Acoustic emission (AE) monitoring has emerged as a valuable tool for damage characterization in cementitious and composite materials. Shen et al. [29] developed a modified statistical constitutive model for tensile–shear damage of sandstone and concrete materials based on acoustic emission clustering under thermo-mechanical coupling, demonstrating that AE cluster analysis can effectively identify tensile–shear damage modes. Su et al. [30]

applied cluster analysis to characterize the tensile damage behavior of 3D C/SiC composites using acoustic emission, validating AE as an important means to reveal internal damage evolution mechanisms in heterogeneous materials. However, these studies focus on thermo-mechanical or ceramic-matrix systems; the application of AE cluster analysis to steel-fiber rubber concrete under room-temperature splitting tension has not been reported. Scanning electron microscopy (SEM) has been widely employed to investigate microstructural damage mechanisms. Chen et al. [31] utilized SEM and NMR to analyze the microstructure evolution of granite residual soil during shearing, demonstrating that SEM can effectively capture particle rearrangement, micro-crack initiation, and interfacial debonding at high resolution. Although focused on geomaterials, the study illustrates the capability of SEM to reveal mesoscopic damage mechanisms in heterogeneous particulate systems, a methodology that has been widely adopted for concrete microstructural analysis. Nevertheless, few studies have applied high-resolution SEM to characterize the specific interfacial transition zones and fiber pull-out traces in steel-fiber rubber concrete after splitting-tensile failure.

The contribution of this study is therefore a structured comparison of 17 tested mixtures spanning four rubber replacement ratios and three steel-fiber volume fractions, evaluated at 7 and 28 days. The mechanical matrix is complemented by failure photographs, representative load-displacement curves, AE energy records for OC, R10C, and SF1RR10C, and qualitative SEM images of selected interfaces and pull-out traces. These modalities are used to compare trends at the specimen scale and to develop a bounded interpretation of possible crack-bridging behavior at the microscopic scale. They are not treated as independent measurements of porosity, bond stress, or statistical interaction.

The specific objectives were to (i) describe how rubber replacement and steel-fiber content relate to the reported 7- and 28-day splitting-tensile strengths; (ii) compare observed failure morphology and representative post-peak response; (iii) interpret the selected AE and SEM observations without extending them beyond their measured scope; and (iv) identify the mixture with the largest reported splitting-tensile strength within the tested matrix.

2. Experimental Scheme Design

Specimen labels follow the rule “SF (steel-fiber volume fraction) RR (rubber replacement ratio) C (concrete)”. SF1RR10C, for example, contains 1% steel fiber and 10% rubber replacement. OC denotes ordinary concrete; R5C denotes rubber concrete with 5% replacement. RC and SFRRC denote rubber concrete and steel-fiber–rubber concrete, respectively.

2.1. Experimental Materials

Tap water and P.O 42.5 ordinary Portland cement (Bagongshan brand; GB 175-2023) [32] were used. Huaihe River sand with a fineness modulus of at least 2.5 was dried and sieved before batching; its apparent and bulk densities were 2489 and 1396 kg/m^3, respectively. The continuously graded crushed stone had a maximum nominal size of 12 mm and apparent and bulk densities of 2780 and 1450 kg/m^3, respectively (Figure 1a,b). The polycarboxylate high-range water-reducing admixture (HPWR-S, standard type; Shanxi Feike New Materials Technology Co., Ltd.; GB 8076-2025 [33], located in Yuncheng City, Shanxi Province, China) was dosed at 1% of the cement mass.

The nominal 40-mesh rubber powder was supplied by Dujiangyan Huayi Rubber Co., Ltd. (located in Chengdu City, Sichuan Province, China) and had a reported density of 1100 kg/m^3. The supplier indices were 92% sieve passage, 0.02% metal, 0.038% fiber, 0.6% moisture, 6% ash, 15% acetone extract, 48% rubber hydrocarbon, and 32% carbon black. Milled low-carbon-steel fibers supplied by Dingsheng Steel Fiber Factory had a diameter of

0.3 mm, length of 30–35 mm (geometric aspect ratio 100–117), density of 7850 kg/m^3, and tensile strength of 680 MPa.

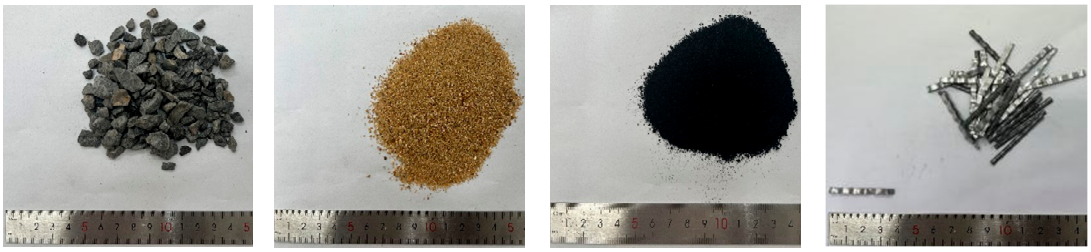

(**a**) crushed stone (**b**) sand (**c**) rubber (**d**) steel fiber

Figure 1. Constituent materials.

2.2. Experimental Design and Specimen Fabrication

The reference mixture followed JGJ 55-2011 [34] with a target mass ratio of cement:fine aggregate:coarse aggregate:water = 1:2:2:0.42; the target water–cement ratio was therefore 0.42, and the water-reducer dosage was held at 1% of cement mass. The archived batch schedule used densities of 3100, 1396, 1450, 1000, 1100, and 7850 kg/m^3 for cement, sand, crushed stone, water, rubber, and steel fiber, respectively. Rubber powder was incorporated by equal-volume replacement of fine aggregates, while steel fibers were added as an external admixture. Seventeen mix proportions were designed with rubber content (5%, 10%, 15%, 20%) and steel fiber volume fraction (0.5%, 1%, 1.5%) as variable factors. The complete 17-mixture proportioning table is provided in Table 1.

Table 1. Complete mix proportions of the 17 mixtures (kg/m^3).

Mixture	Cement	Sand	Crushed Stone	Rubber	Steel Fiber	Water	Admixture
OC	380.95	761.90	761.90	0.00	0.00	160.00	3.81
R5C	380.95	723.81	761.90	30.02	0.00	160.00	3.81
R10C	380.95	685.71	761.90	60.04	0.00	160.00	3.81
R15C	380.95	647.62	761.90	90.05	0.00	160.00	3.81
R20C	380.95	609.52	761.90	120.07	0.00	160.00	3.81
SF0.5RR5C	380.95	723.81	761.90	30.02	39.25	160.00	3.81
SF1RR5C	380.95	723.81	761.90	30.02	78.50	160.00	3.81
SF1.5RR5C	380.95	723.81	761.90	30.02	117.75	160.00	3.81
SF0.5RR10C	380.95	685.71	761.90	60.04	39.25	160.00	3.81
SF1RR10C	380.95	685.71	761.90	60.04	78.50	160.00	3.81
SF1.5RR10C	380.95	685.71	761.90	60.04	117.75	160.00	3.81
SF0.5RR15C	380.95	647.62	761.90	90.05	39.25	160.00	3.81
SF1RR15C	380.95	647.62	761.90	90.05	78.50	160.00	3.81
SF1.5RR15C	380.95	647.62	761.90	90.05	117.75	160.00	3.81
SF0.5RR20C	380.95	609.52	761.90	120.07	39.25	160.00	3.81
SF1RR20C	380.95	609.52	761.90	120.07	78.50	160.00	3.81
SF1.5RR20C	380.95	609.52	761.90	120.07	117.75	160.00	3.81

Rubber powder was incorporated by equal-volume replacement of fine aggregate. The replacement ratio RR (%) defines the volume of rubber powder equal to RR% of the original fine aggregate volume in the reference mixture. Based on the archived batch-schedule density of 1396 kg/m^3 for sand and 1100 kg/m^3 for rubber, the rubber mass was calculated as follows: $m_{rubber} = \frac{RR\% \times m_{sand,0}}{\rho_{sand,bulk}} \times \rho_{rubber} = \frac{RR\% \times 761.90}{1396} \times 1100$, and the remaining fine aggregate mass was $m_{sand} = m_{sand,0} - \frac{RR\% \times m_{sand,0}}{\rho_{sand,bulk}} \times \rho_{sand,bulk} = (1 - RR\%) \times 761.90$.

Steel fibers were added as an external admixture by volume fraction, with mass $m_{fiber} = V_{fiber} \times 7850$ kg/m^3.

For each batch, the weighed sand, crushed stone, rubber, and steel fibers were dry-mixed for 30 s. Cement was then added and mixed for 1 min. Water and the dissolved water-reducing admixture were added, followed by 2 min of mixing. The mixture was placed into the mold in one lift, rodded along the inner mold surface, and compacted on a vibrating table until visible surface bubbles ceased. Vibration was then stopped to limit fiber or coarse-aggregate settlement and paste rise. The surface was struck off, and the specimens were labeled by mixture.

Specimen curing followed GB/T 50081-2019 [35]. The molds were fully covered by plastic film after casting to mitigate water evaporation. The specimens were demolded after 2d, sprayed with water and wrapped in plastic film, and cured at 20 °C ± 2 °C, with relative humidity exceeding 90%, up to 7d and 28d. The moisturized specimens were taken out one day prior to testing, cleaned, and placed in indoor air for 24 h.

Figure 2 summarizes the material preparation, splitting test, AE acquisition, and SEM observation workflow.

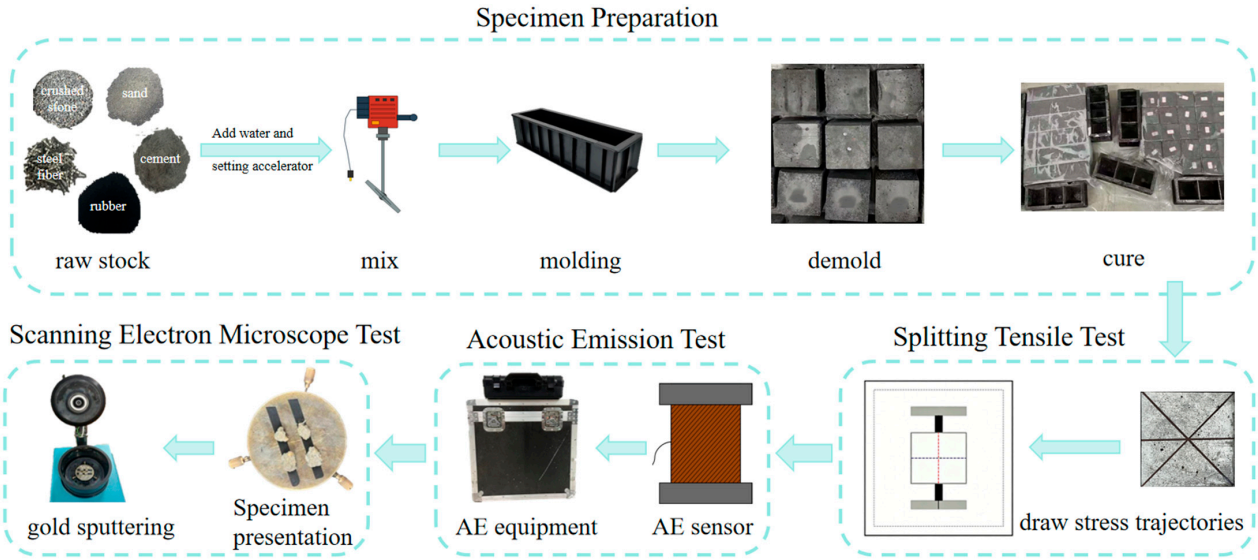

Figure 2. Specimen preparation and test procedures.

Figure 2 depicts the research workflow from constituent proportioning and specimen preparation through splitting-tensile testing, synchronized AE monitoring, and post-test SEM observation. The diagram identifies the sequence of the three evidence streams used in this study.

2.3. Experimental Equipment

Splitting tests were conducted with an RMT-150B rock-mechanics testing system. (Manufactured by the Institute of Rock and Soil Mechanics, Chinese Academy of Sciences, Wuhan, China). The SEM observations used a FlexSEM 1000 II instrument (Manufactured by Hitachi High-Technologies Corporation, Tokyo, Japan), whose stated resolution is 4.0 nm

at 20 kV. The AE data were acquired with a full-information system supplied by Soft Island Technology (Located in Chongqing, China). Figure 3 identifies the loading system, fixture, specimen, and sensor arrangement. The specimen is subjected to opposing compressive line loads that generate transverse tensile stress along the loaded diameter.

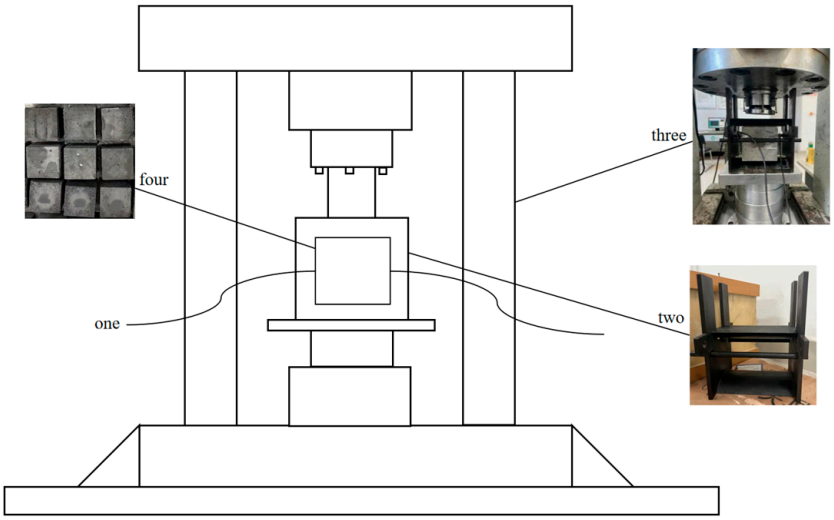

Figure 3. Splitting-tensile test equipment and specimen arrangement. Notes: 1—AE sensor; 2—splitting-test fixture; 3—RMT-150B loading system; 4—concrete specimen.

2.4. Splitting-Tensile Test and Displacement Acquisition

The splitting-tensile tests used 100 × 100 × 100 mm cube specimens in a custom fixture mounted in an RMT-150B testing system. Loading lines were marked on the specimen. Wooden bearing strips were placed at the upper and lower loading lines, an equal-size steel plate was positioned above the specimen, and the specimen, fixture, and loading lines were aligned before loading at a cross-head rate of 3 mm/min. The bearing strips are made of hardwood with dimensions of 25 mm (width) × 12 mm (thickness) × 150 mm (length), complying with ASTM C496 [36]. The loading was performed under displacement-control mode. The termination criteria were full specimen failure or a load drop below 20% of the peak load. Two symmetrically arranged LVDTs (range ±5 mm, accuracy 0.001 mm) were mounted to measure the relative lateral displacement of the specimen. These LVDT data were used solely for machine-compliance calibration: standard steel specimens were tested to establish the machine-compliance correction, which was applied to the LVDT records to verify specimen deformation.

The archived protocol prepared three parallel specimens per mixture; a result differing by more than ±15% from the group mean was treated as an outlier, and a replacement specimen was prepared and tested.

2.5. Acoustic-Emission Monitoring and SEM Observation

Before loading, the specimen surface was cleaned, petroleum jelly was applied as a couplant, and the AE sensor was secured with adhesive tape. Data were acquired with a full-information AE system supplied by Soft Island Technology. Table 2 lists the AE parameters.

Table 2. Acoustic emission (AE) parameters.

Parameters	Specifications
Sensor model	PAC Nano30 (Physical Acoustics Corporation)
Operating frequency range	125–750 kHz

Table 2. *Cont.*

Parameters	Specifications
Resonant frequency	140 kHz
Preamplifier gain	40 dB
Threshold	40 dB
Sampling rate	1 MS/s
Acquisition parameters	Peak definition time (PDT) = 40 μs, hit definition time (HDT) = 80 μs, hit lockout time (HLT) = 300 μs
Filter	Band-pass filter: 125 kHz high-pass, 1 MHz low-pass
Sensor arrangement	Two sensors were symmetrically mounted at the mid-height of specimen side surfaces with spacing of 100 mm
Channel number	CH1 (left side), CH2 (right side)
Calibration procedure	The pencil-lead break method (Hsu–Nielsen source) was adopted for simulated-source calibration on the specimen surface, ensuring that the arrival-time difference of signals from the two sensors was within ±2 μs.

Small blocks were taken from the tested specimens, vacuum-dried to remove moisture and loose contamination, and sputter-coated with a 5–10 nm gold layer before imaging with a FlexSEM 1000 II. The instrument has a stated resolution of 4.0 nm at an accelerating voltage of 20 kV.

3. Analysis of Experimental Results

3.1. Data Analysis of Experimental Results

Table 3 presents the splitting tensile strength values of three replicates for 17 mixtures at curing ages of 7 days and 28 days. For groups containing merely three parallel specimens, we re-evaluated the data and decided against direct elimination of suspected outliers. The Grubbs' outlier test (significance level $\alpha = 0.05$) was therefore applied. Only two valid values were available for the OC group at 7d. A measured result was defined as an outlier if its deviation from the group mean exceeded ±15%. Additional specimens were cast and retested.

The outlier treatment followed a two-stage sequential protocol. Stage 1 (screening): For each group of three parallel specimens, any result deviating by more than ±15% from the provisional group mean was flagged as a suspected outlier. Stage 2 (confirmation): Grubbs' test ($\alpha = 0.05$, two-sided) was then applied to the remaining values. A specimen was excluded and replaced only if it failed both criteria. For the 7-day OC group, one original specimen deviated by +16.2% from the mean of the other two and also yielded a Grubbs G-statistic exceeding the critical value ($G > G_{crit}$). It was therefore excluded, a replacement specimen was cast from the same batch and cured under identical conditions, and the final mean and standard deviation in Table 4 are based on the three valid specimens. No outliers were detected in any other group.

(1) For mixtures without steel fibers, the reported splitting-tensile strength decreased as the rubber replacement increased. Relative to OC, R5C was 4.1% lower at 7 days and 2.1% lower at 28 days, whereas R20C was 38.2% lower at 7 days and 19.0% lower at 28 days. These observations are consistent with a lower-stiffness rubber phase and a comparatively weak rubber–paste interface, but the air content and porosity were not measured and therefore are not asserted as demonstrated causes.

Table 3. Splitting tensile strength values of three replicates per group.

Number	Splitting Tensile Strength/MPa						Concrete Type
	7 d			28 d			
OC	3.10	3.14	3.18	3.78	3.80	3.82	reference concrete
R5C	2.98	3.01	3.04	3.65	3.72	3.79	rubber concrete
R10C	2.72	2.76	2.80	3.41	3.44	3.47	
R15C	2.69	2.74	2.79	3.23	3.25	3.27	
R20C	1.86	1.94	2.02	3.02	3.08	3.14	
SF0.5RR5C	3.25	3.31	3.37	4.01	4.06	4.11	steel-fiber–rubber concrete
SF1RR5C	3.42	3.46	3.50	4.25	4.27	4.29	
SF1.5RR5C	2.84	2.87	2.90	3.76	3.80	3.84	
SF0.5RR10C	3.19	3.25	3.31	4.02	4.08	4.14	
SF1RR10C	3.41	3.45	3.49	4.06	4.11	4.16	
SF1.5RR10C	2.69	2.74	2.79	3.93	3.99	4.05	
SF0.5RR15C	3.11	3.14	3.17	3.83	3.87	3.91	
SF1RR15C	3.02	3.09	3.16	3.71	3.78	3.85	
SF1.5RR15C	2.66	2.69	2.72	3.51	3.54	3.57	
SF0.5RR20C	2.75	2.76	2.77	3.56	3.61	3.66	
SF1RR20C	2.56	2.62	2.68	3.60	3.66	3.72	
SF1.5RR20C	2.28	2.33	2.38	3.47	3.51	3.55	

Table 4. Reported splitting-tensile strength values.

Number	Mean Value of Strength/MPa		Standard Deviation		Number of Valid Samples		Concrete Type
	7 d	28 d	7 d	28 d	7 d	28 d	
OC	3.14	3.8	0.04	0.02	3	3	reference concrete
R5C	3.01	3.72	0.03	0.07	3	3	rubber concrete
R10C	2.76	3.44	0.04	0.03	3	3	
R15C	2.74	3.25	0.05	0.02	3	3	
R20C	1.94	3.08	0.08	0.06	3	3	
SF0.5RR5C	3.31	4.06	0.06	0.05	3	3	steel-fiber–rubber concrete
SF1RR5C	3.46	4.27	0.04	0.02	3	3	
SF1.5RR5C	2.87	3.8	0.03	0.04	3	3	
SF0.5RR10C	3.25	4.08	0.06	0.06	3	3	
SF1RR10C	3.45	4.11	0.04	0.05	3	3	
SF1.5RR10C	2.74	3.99	0.05	0.06	3	3	
SF0.5RR15C	3.14	3.87	0.03	0.04	3	3	
SF1RR15C	3.09	3.78	0.07	0.07	3	3	
SF1.5RR15C	2.69	3.54	0.03	0.03	3	3	
SF0.5RR20C	2.76	3.61	0.01	0.05	3	3	
SF1RR20C	2.62	3.66	0.06	0.06	3	3	
SF1.5RR20C	2.33	3.51	0.05	0.04	3	3	

Notes: OC, ordinary concrete; R5C, concrete with 5% rubber replacement; SF0.5RR5C, concrete with 0.5% steel fiber and 5% rubber replacement.

(2) Within the tested rubber-containing mixtures, the largest reported values were observed at 0.5% or 1.0% steel fiber. SF1RR5C recorded the highest strength at both ages (3.46 MPa at 7 days and 4.27 MPa at 28 days), corresponding to descriptive increases of 10.2% and 12.4% over OC. At 1.5% steel fiber, the reported strength was lower than that at 1.0% for each rubber level. It should be emphasized that the tested fiber contents are discrete levels (0.5%, 1.0%, 1.5%) and no intermediate levels were evaluated; therefore, the observed trend does not permit interpolation or identification of an optimum. The lower strength at 1.5% is hypothesized to result from reduced workability, fiber balling, entrapped

air, or compaction difficulty at high fiber content, as proposed in the literature [22,24,37]. These mechanisms are plausible explanations but were not directly measured or verified in this study.

Both 7- and 28-day strength values are retained in Table 2 and Figure 4. The detailed load-displacement discussion focuses on 28-day specimens because they provide a mature-age comparison and reduce duplication after the two ages showed the same qualitative ordering in the available curves. This selection does not imply that the 7-day results were discarded; the early-age values remain part of the mechanical comparison.

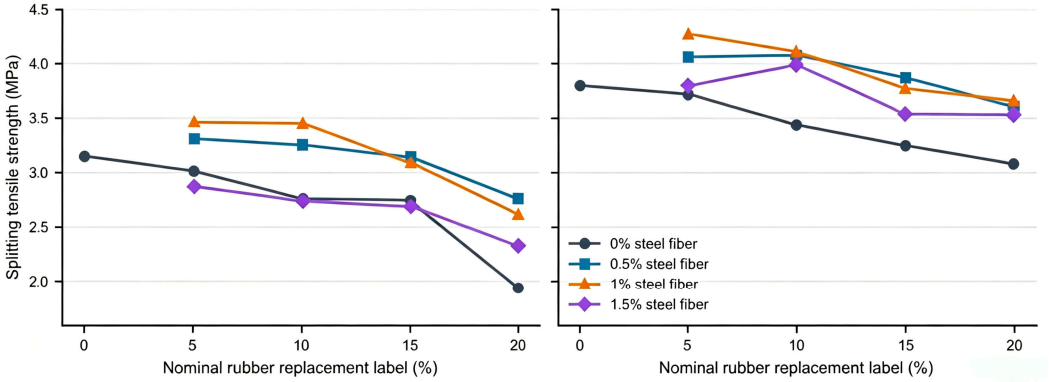

(**a**) 7-day splitting strength (**b**) 28-day splitting strength

Figure 4. Reported splitting-tensile strength across rubber replacement and steel-fiber contents at (**a**) 7 days and (**b**) 28 days.

3.2. Analysis of Specimen Failure Modes

Figure 5 shows that OC, rubber concrete (RC), and steel-fiber–rubber concrete (SFRRC) developed a dominant splitting crack approximately parallel to the applied compressive line load.

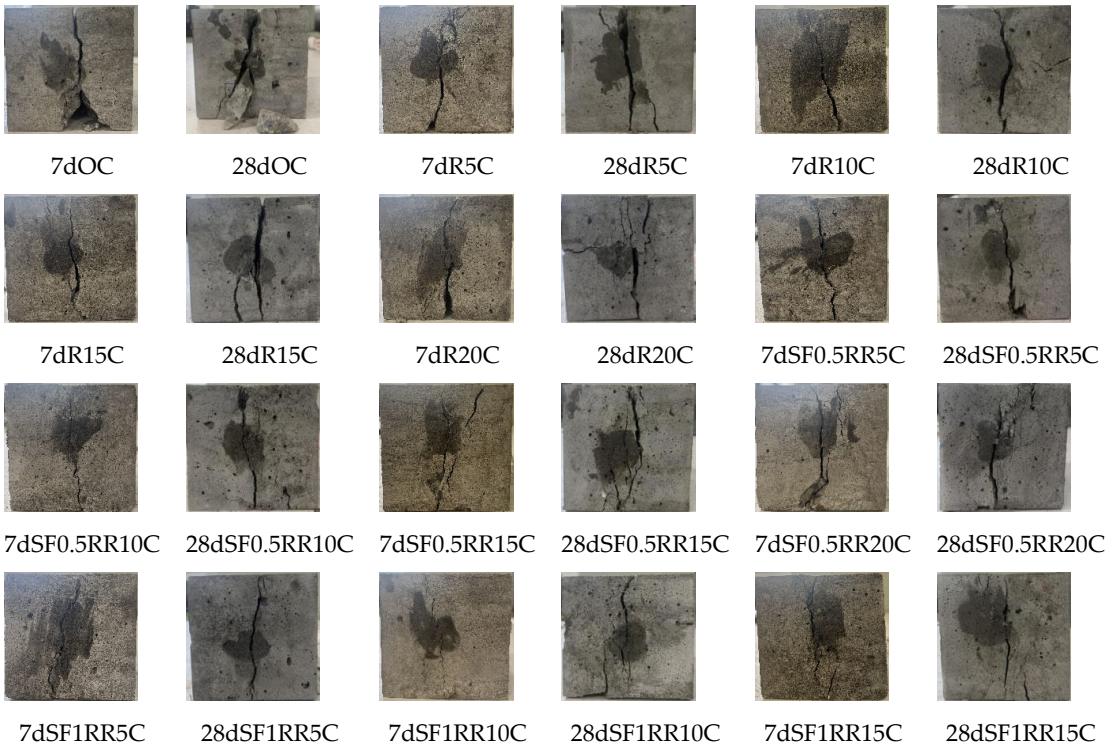

Figure 5. *Cont.*

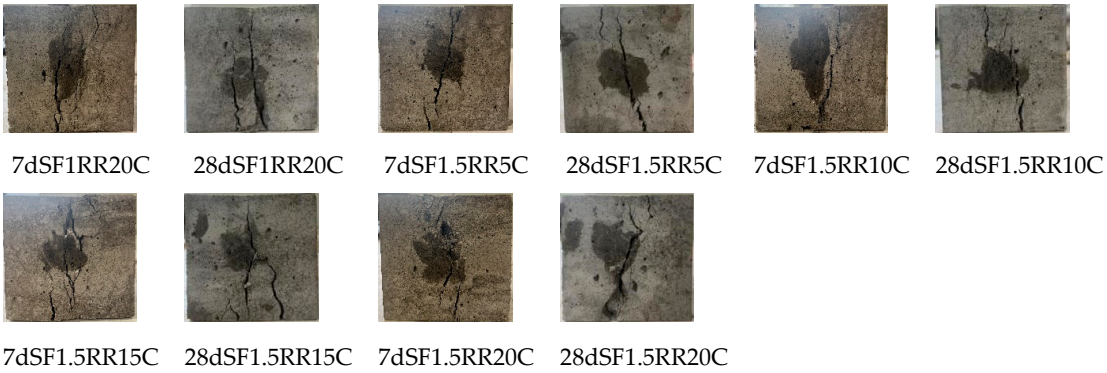

Figure 5. Failure patterns of 7d and 28d splitting tensile specimens.

(1) OC and RC separated abruptly near the peak load in the photographed tests, whereas the fiber-containing specimens retained greater post-test integrity. The observations are described as delayed separation and gradual post-peak softening, not plastic failure, because irreversible plastic strain was not measured.

(2) Fibers are visible crossing the crack surfaces in the photographs. This observation is qualitatively consistent with the residual load capacity observed in the load-displacement curves, but the photographs do not identify which fibers were load-bearing, nor do they quantify pulled-out versus fractured fractions, embedded length, pull-out energy, bond stress, or the relative contributions of adhesion, friction, and mechanical anchorage.

3.3. Load-Displacement Curve Analysis

The available 7- and 28-day splitting-test curves showed similar qualitative ordering, so Figure 6 presents the 28-day curves to focus the comparison at mature age. The plotted displacement is the RMT-150B system displacement.

However, the load–displacement curves presented in Figure 6 use the raw system displacement recorded by the RMT-150B cross-head because the corrected LVDT data exhibited localized scatter near peak load due to crack-induced surface rotation and irregular crack opening along the loaded diameter, making them unsuitable for direct curve plotting without additional fracture-mechanics interpretation (e.g., crack-mouth opening displacement, CMOD). Consequently, the displacements plotted in Figure 6 represent the machine cross-head movement and include machine compliance; they are intended for qualitative comparison of post-peak trends only. The splitting-tensile strength was calculated as $f_{ts} = 2F/(\pi A)$, where F is the peak load (N) and A is the nominal splitting area (mm^2).

Displacement data and scope of interpretation. The load–displacement curves in Figure 6 are plotted using the raw system displacement recorded by the testing-machine cross-head. While LVDTs were installed to measure relative lateral displacement and machine compliance was calibrated, the corrected LVDT records were not used for Figure 6 because crack-induced surface rotation and non-uniform crack opening along the loaded diameter produced localized scatter that complicates direct curve interpretation. The system displacement therefore includes machine compliance and should be interpreted as a qualitative indicator of the post-peak softening rate and residual load retention, not as a quantitative measure of specimen deformation, crack opening, or energy absorption. Comparisons among the mixtures (e.g., more gradual load decay in the fiber-containing specimens) are valid as qualitative observations of failure-mode differences; they do not establish quantitative rankings of ductility or fracture energy.

For Figure 6, the displayed curve for each mixture is the raw load–displacement record of the single specimen whose peak load was closest to the group mean of the three parallel

tests. Figure 6 presents one unprocessed curve per mixture for illustrative purposes only; it does not claim to represent the within-group variability in the post-peak response.

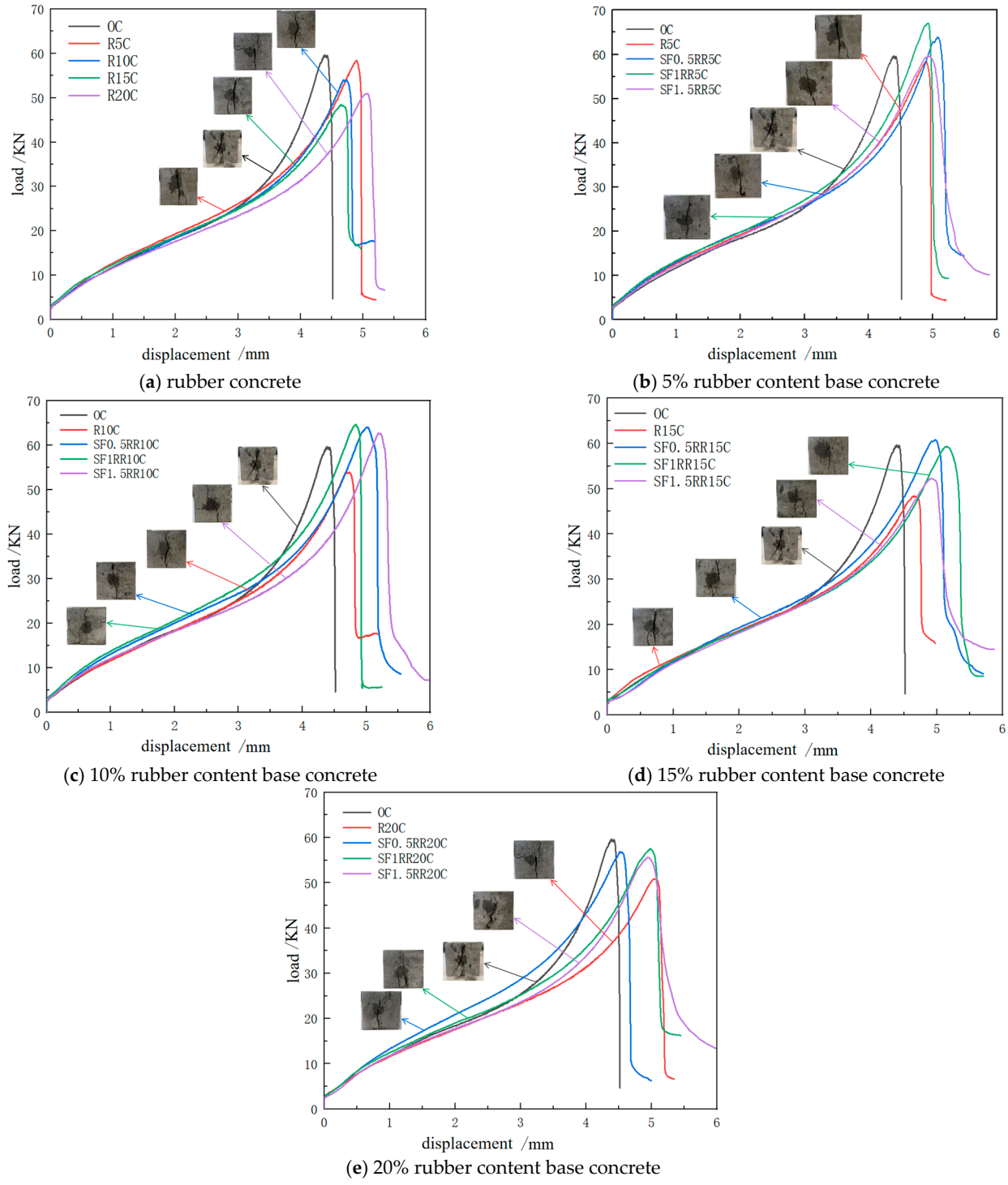

(**a**) rubber concrete

(**b**) 5% rubber content base concrete

(**c**) 10% rubber content base concrete

(**d**) 15% rubber content base concrete

(**e**) 20% rubber content base concrete

Figure 6. Representative 28-day load-system-displacement curves from the splitting-tensile tests.

Figure 6 presents the load-system displacement curves and post-failure morphologies of specimens with various mix proportions under monotonic loading. It should be noted that the displacements plotted in the figure are the system displacements recorded by the testing-machine cross-head, which include machine compliance. No independent calibration of crack-mouth opening displacement (CMOD) or fracture-energy measurements were performed.

For the rubber-only replacement series (Figure 6a), the load of the OC specimen drops sharply after reaching the peak load, and a single penetrating main crack can be observed after failure. As the rubber replacement ratio increases from 5% to 20%, the peak loads of the rubber-modified concrete specimens decrease relative to OC. Meanwhile, the post-peak load-descending branches become more gradual to varying degrees compared with OC. Macroscopic observations after failure reveal more cracks on the surfaces of the rubber-modified concrete specimens than on the OC, and some cracks exhibit visible branching near rubber particles.

In the steel-fiber–rubber concrete series (Figure 6b–e), specimens reinforced with steel fibers generally exhibit a visually gentler post-peak load drop in the system-displacement records compared with reference specimens at identical rubber replacement ratios. Some specimens retain visually detectable residual load at large system displacements. These observations describe the recorded system response and do not quantify specimen deformation or energy absorption. These observations describe differences in recorded load-displacement behavior and post-failure geometric integrity; they do not, in the absence of fracture-energy or CMOD measurements, establish quantitative improvements in material toughness or ductility. The post-failure photographs show fiber-pull-out traces on the fracture surfaces of the steel-fiber-reinforced specimens, together with multiple visible surface cracks. Notably, at the 20% rubber replacement ratio (Figure 6e), the improvement in post-peak load retention provided by the steel fibers is weakened relative to the 5–15% replacement series. This observation is limited to the single-load response shown in Figure 6 and does not predict behavior under cyclic or repeated loading.

Given that the displacement data are system displacements and independent CMOD or fracture-energy measurements are unavailable, the curve shapes and crack photographs in Figure 6 only reflect differences in failure modes among specimens of different mix proportions. Quantitative inferences regarding the enhancement of ductility or toughness should not be drawn solely from these results.

3.4. Acoustic Emission (AE) Energy Characteristics

AE records transient elastic waves associated with rapid local energy release. Recorded AE energy is an indirect, system-dependent signal influenced by source activity, attenuation, impedance contrast, threshold, sensor placement, coupling, and waveform processing; it is therefore not a direct measure of crack volume or internal damage [38]. In this study, the four stages are retained as a descriptive segmentation of the synchronized load-energy records rather than as statistically detected change points.

Stage 1 (low recorded activity): The applied load increases while recorded AE energy remains low under the selected threshold.

Stage 2 (gradual recorded activity): The recorded AE energy increases as visible or internal cracking activity develops.

Stage 3 (rapid recorded activity): The recorded energy rate increases sharply near peak load, coinciding with the visible development of a splitting crack in the tested specimens. The AE record alone does not establish a unique physical cause for the energy increase.

Stage 4 (post-peak response): The load decreases while recorded activity continues. Possible sources of this activity include ongoing micro-fracture or frictional processes at the crack surfaces, but these mechanisms are not independently verified by the AE measurement alone.

Figure 7 compares OC, R10C, and SF1RR10C to provide a controlled qualitative sequence from ordinary concrete to 10% rubber concrete and then to the same rubber content with 1% steel fiber. The AE interpretation is restricted to these three displayed mixtures.

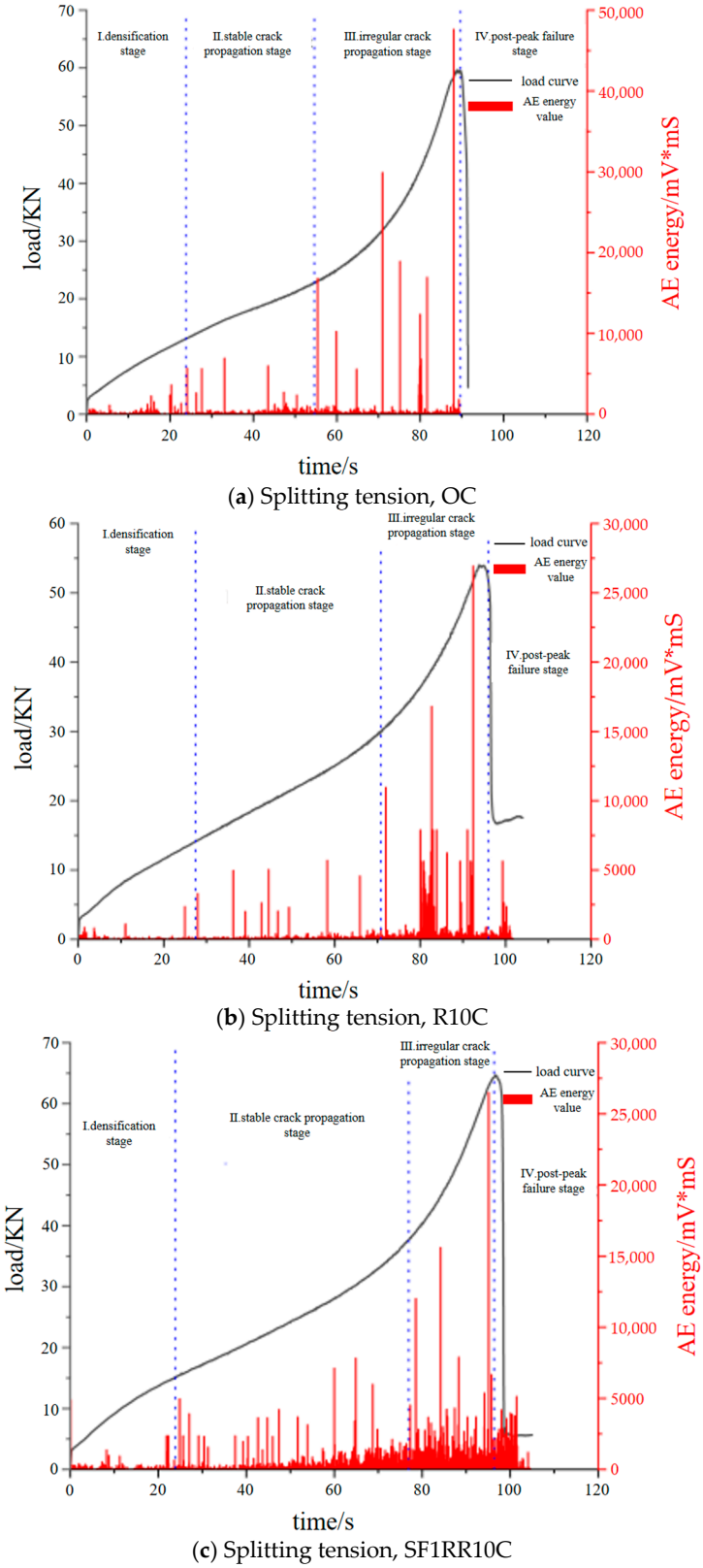

Figure 7. Load and recorded AE energy versus time for OC, R10C, and SF1RR10C. (The right Y-axis denotes AE energy, and its unit is mV*mS).

(1) The displayed rubber-containing curves show longer low-activity and gradual-growth intervals than OC under the stage definitions used here. This difference is descriptive and mixture-specific.

(2) Lower recorded AE energy in R10C and SF1RR10C cannot by itself demonstrate less internal damage because rubber particles, interfaces, voids, and fibers can alter wave transmission and sensor response. The curves are therefore interpreted as different recorded AE responses rather than quantitative damage rankings.

(3) Continued post-peak recorded activity in the displayed SF1RR10C record coincides with the maintenance of residual load. This activity may reflect ongoing micro-fracture or frictional processes at crack surfaces; however, the AE signal does not distinguish among specific mechanisms such as fiber pull-out, interfacial slip, or matrix cracking.

4. Toughening Mechanism of Steel-Fiber-Reinforced Concrete

4.1. Macroscopic Interpretation Under Splitting Tension

Figure 8a compares the photographed post-test states of OC and SF1RR5C. The fiber-containing specimen retained greater post-test geometric integrity than OC, with fibers visibly spanning the crack opening. This morphology is compatible with the residual load capacity recorded by the testing machine, but the photograph does not independently verify load transfer across the crack or distinguish between active bridging and passive fiber embedment. From a methodological perspective, the qualitative interpretation of fiber bridging based on post-failure photographs and system-displacement curves has well-known limitations: without measured bond–slip laws or pull-out force–displacement curves, the contribution of individual fibers to crack resistance cannot be quantified. Analytical models for the pull-out behavior of multi-hook-end steel fibers in cementitious matrices demonstrate that fiber geometry, embedment length, and interfacial bond govern the energy dissipated during pull-out; the present study does not measure these parameters and therefore does not claim a quantitative toughening effect. The comparison is qualitative and does not establish a measured bond law or a statistically optimized mixture.

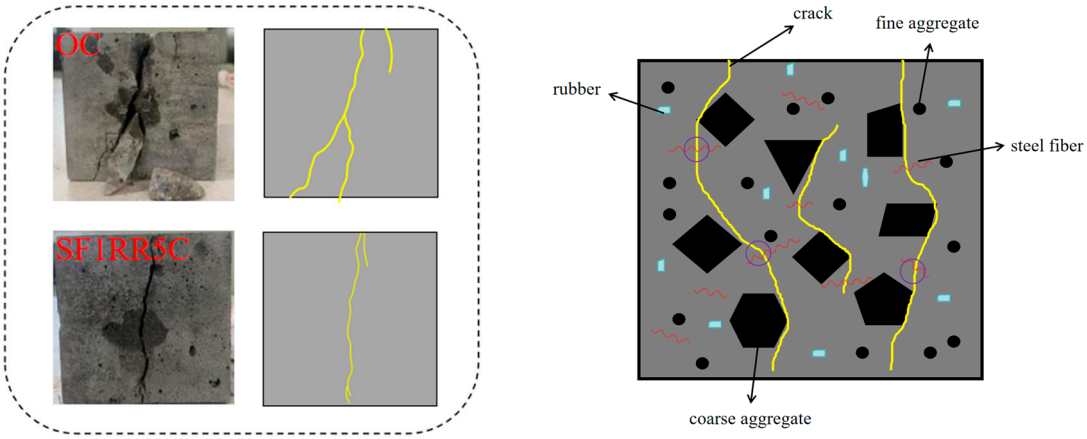

(**a**) Comparison of failure modes in mechanical tests (**b**) Steel fiber crack resistance model

Figure 8. Macroscopic mechanism of steel-fiber-toughened concrete.

Figure 8b has been reinterpreted for the Brazilian splitting configuration. Opposing compressive line loads generate a transverse tensile stress field near the loaded diameter, and a dominant splitting crack develops approximately parallel to the loading direction. Fibers that intersect the developing fracture process zone can transfer tensile traction across the crack through adhesion, friction, and mechanical anchorage, thereby delaying complete separation and contributing to residual load.

Figure 9 shows fibers intersecting the fracture surface and traces exposed by manual separation. Steel fibers are visibly distributed across the fracture surfaces, a morphology that is commonly associated with fiber bridging in the literature. The photographs do not,

however, establish that these fibers were load-bearing during the test or quantify their contribution to crack resistance. As shown in Figure 9a, steel fiber surfaces are partially covered with cement-paste residue after failure, suggesting that some degree of adhesion existed between the fiber and the matrix. This observation alone does not determine bond strength or the fiber's contribution to peak load. After peak load, the fiber-containing specimens remained visibly connected rather than separating into discrete pieces during manual handling. This post-failure integrity is an observed geometric state, not a measured toughness or energy-absorption value. After manual separation attempts, some steel fibers remained visibly connecting the two halves of the specimen when lifted vertically. This post-failure integrity is qualitatively consistent with fiber bridging, but the photograph does not quantify anchorage strength, pull-out energy, or fiber stiffness. Figure 9c shows the steel fibers still embedded in the concrete matrix after manual separation. The photographs display the fiber location and surface coverage by matrix material but do not quantify anchorage strength, mechanical interlock, or bond stress. These macroscopic images show steel fibers crossing the visible crack surfaces, which is qualitatively consistent with the residual load capacity observed in the load-displacement curves. The photographs alone do not establish quantitative contributions to crack resistance or energy absorption; in particular, without measured pull-out force–displacement relationships or fracture-energy values, no quantitative inference regarding toughness improvement or brittleness reduction can be drawn.

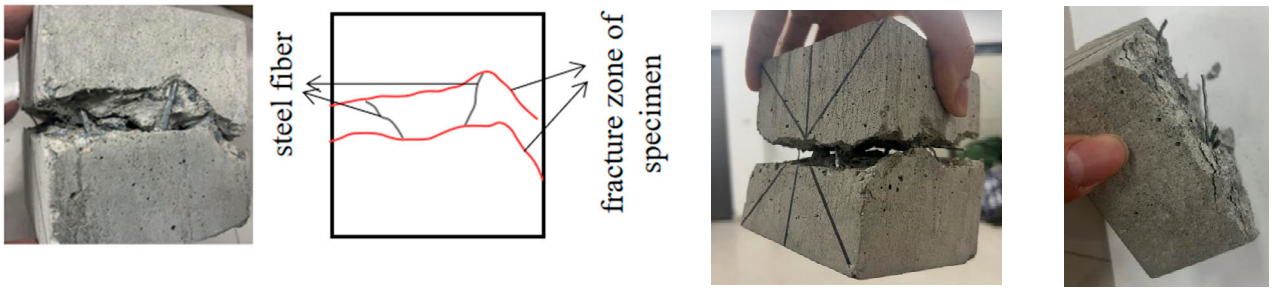

(**a**) Internal failure details of specimens (**b**) Bridging effect (**c**) Fracture morphology

Figure 9. Detailed views of splitting tensile failure.

4.2. Microscopic Mechanism

Most studies on the performance and mechanism of composite concrete materials are based on macroscopic analysis of mechanical test results. In fact, concrete is a heterogeneous material and becomes more complex after adding one or more components to form composites. The differences in mechanical response observed in the macroscopic tests are associated with internal structural changes at the microscale.

As shown in the micrograph (Figure 10a), the interfacial transition zone between steel fibers and cement paste contains visible gaps; some regions show cement-paste residue adhering to the fiber surface. Figure 10b,c show micrographs of steel fiber pull-out traces with scattered micro-cracks visible on the trace surfaces. These micro-cracks are observed features of the post-mortem fracture surface; the SEM images do not capture the dynamic stress redistribution process during loading. The pull-out trace surfaces appear rough under SEM observation, with cement-paste debris visible on the fiber surface. This morphology is consistent with the removal of interfacial material during fiber extraction and with the qualitative concept of fiber bridging commonly discussed in the literature. However, the SEM image alone does not quantify interfacial shear strength, frictional resistance, bond energy, pull-out force, or the energy dissipated during fiber extraction.

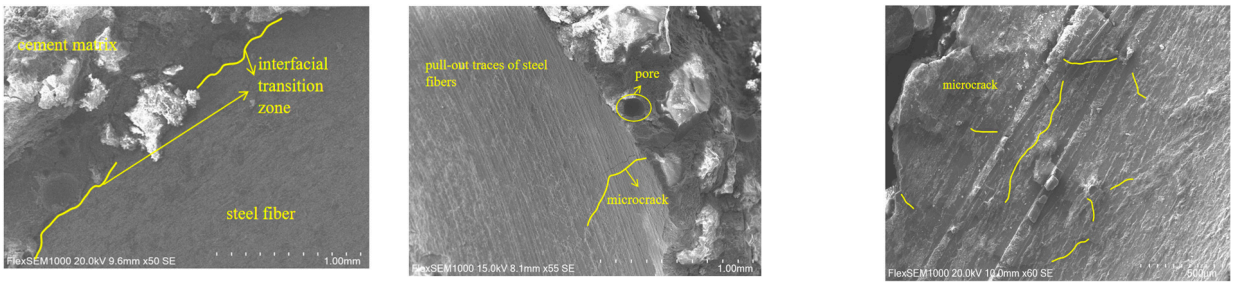

(**a**) interfacial transition zone (**b**) pull-out traces of steel fibers (**c**) Micro-morphology of pulled-out steel fibers

Figure 10. Microstructure of steel fiber rubber concrete.

Scope and Limitations of the SEM Interpretation. The SEM micrographs in Figure 10 provide qualitative, post-mortem morphological evidence of fiber–matrix interaction. The cement-paste residue visible on some fiber surfaces (Figure 10a) and the rough texture of pull-out traces (Figure 10b,c) are consistent with the occurrence of interfacial adhesion and material removal during fiber extraction. However, these observations are inherently limited to geometric features preserved after failure. They do not—and cannot—quantify the interfacial shear strength, local bond stress, frictional resistance during pull-out, mechanical anchorage capacity, or the energy dissipated in the fracture process. Quantification of these parameters requires dedicated interface-characterization experiments that were outside the scope of this study, such as single-fiber pull-out tests with synchronized force–displacement recording, nanoindentation traverses across the interfacial transition zone, or in situ SEM micromechanical testing with calibrated load cells. Methodologically, the transition from qualitative imaging to quantitative bond-property determination has been addressed through finite-element and machine-learning frameworks that integrate interfacial constitutive laws to predict bond stress–slip behavior of steel bars in concrete under static and dynamic loading. These approaches illustrate the substantial gap between descriptive microstructural imaging and the measurement of interface properties necessary to validate quantitative toughening claims. The SEM discussion in this manuscript is therefore strictly bounded to descriptive microstructural observations, and no quantitative bond-law, anchorage-strength, or energy-dissipation claims are made.

4.3. Scope and Limitations

This study has two principal limitations. First, no steel-fiber-only mixtures were included, so the independent fiber effect and a full rubber–fiber interaction cannot be estimated across the design space. Second, the AE comparison covers only the three displayed mixtures, and the SEM analysis is qualitative; neither method directly quantifies internal damage or bond strength.

5. Conclusions

(1) The mixtures carrying nominal RR5-RR20 rubber labels showed progressively lower splitting-tensile strength in the absence of steel fibers. Relative to OC, the reported R5C reductions were 4.1% at 7 days and 2.1% at 28 days, whereas R20C was 38.2% and 19.0% lower, respectively.

(2) Within the tested matrix of 17 mixtures, the reported splitting-tensile strengths at both 7 and 28 days exhibited a non-monotonic trend with respect to the steel-fiber volume fraction. The largest measured values occurred at 0.5% and 1.0% steel fiber for each rubber replacement level, whereas the values at 1.5% fiber content were consistently lower than those at 1.0%. Among the tested combinations, SF1RR5C (1% steel-fiber volume fraction, 5% rubber replacement ratio) recorded the highest 28-day splitting-tensile strength of 4.27 MPa,

which is 12.4% higher than that of the ordinary concrete (OC). This observation is strictly descriptive of the 17 tested mixtures and the tested fiber contents (0.5%, 1.0%, 1.5%); it does not establish a statistically optimized global optimum, nor does it exclude the possibility that an intermediate fiber content between the tested levels (e.g., 0.75%) could yield a higher strength. The experimental program did not include a formal optimization framework (e.g., response-surface methodology) or inferential statistical comparison (e.g., ANOVA with post hoc testing); therefore, statements regarding the "best" fiber content are avoided. These are descriptive observations of peak strength only. This study did not measure fracture energy, CMOD-based toughness indices, or equivalent quantitative parameters; therefore, no conclusion is drawn regarding improvements in material toughness, ductility, or fracture resistance.

(3) The displayed single-specimen load-displacement curves and failure photographs visually indicate more gradual post-peak softening, residual load, and delayed separation in the fiber-containing mixtures tested. These qualitative observations describe differences in post-peak behavior and failure morphology; they do not establish quantitative improvements in toughness or ductility in the absence of fracture-energy or CMOD measurements.

(4) The selected AE records and SEM images are qualitatively consistent with mixture-dependent cracking and fiber bridging, but recorded AE energy is not a direct damage measure, and the SEM images do not quantify porosity or bond strength. The findings are limited to the displayed AE groups, selected micrographs, and unconditioned laboratory specimens.

(5) All the reported results are strictly limited to monotonic splitting-tensile tests on unconditioned laboratory specimens cured under standard temperature and humidity. They do not establish durability under environmental exposure (freeze–thaw, thermal cycling, chemical attack), performance under sustained or cyclic loading, or long-term field behavior. The mechanical baseline reported here may serve as a reference for future studies investigating these environmental and loading effects. All the mechanical results were obtained from monotonic splitting-tensile tests. The observed post-peak residual load and delayed separation describe the single-load response of unconditioned laboratory specimens and do not establish fatigue life, cyclic degradation characteristics, or dynamic performance. Extension to cyclic or repeated loading regimes is identified as a necessary direction for future research.

Author Contributions: A.L. was responsible for conceptualization, test scheme design, specimen preparation, experimental testing, formal data analysis, microscopic characterization, visualization and original draft writing. N.X. contributed to conceptualization, research supervision, project administration, funding acquisition, manuscript review and editing. C.S. took charge of methodology optimization, mechanical performance verification, technical discussion and manuscript revision. Y.Z. assisted in data curation, acoustic emission data processing and partial manuscript polishing. All authors have read and agreed to the published version of the manuscript.

Funding: This work was supported by the National Natural Science Foundation of China (Grant No. 52374156).

Institutional Review Board Statement: Not applicable.

Informed Consent Statement: Not applicable.

Data Availability Statement: The original contributions presented in this study are included in the article. Further inquiries can be directed to the corresponding author.

Conflicts of Interest: The authors declare no conflicts of interest.

References

1. Wang, W.; Hong, Y.L.; Jiang, P.; Zhan, H.H.; Ren, T.X.; Qiu, X.R.; Li, C.H. Research progress of basalt fiber reinforced concrete: Mechanical properties, durability, microscopic mechanism. *J. Compos. Sci. Technol.* **2026**, *14*, 1–27. [CrossRef]
2. Wu, T.; Xiao, Z.Y.; Wei, H.; Zhang, J.G. Experimental Study on Bond Performance and Crack Width of High-Strength Steel Bar High-Strength Lightweight Aggregate Concrete Beam Members. *Eng. Mech.* **2026**, 1–14. Available online: https://link.cnki.net/urlid/11.2595.O3.20250723.1001.032 (accessed on 13 March 2026).
3. Wang, Y.H.; Nejati, F.; Edalatpanah, S.A.; Karim, R.G. Experimental study to compare the strength of concrete with different amounts of polypropylene fibers at high temperatures. *Sci. Rep.* **2024**, *14*, 8566. [CrossRef] [PubMed]
4. Shi, J.J.; Li, T.X.; Liu, L.; Zeng, D.C. Impact resistance evaluation of chopped carbon fiber concrete based on two-parameter Weibull distribution. *J. Compos. Sci. Technol.* **2026**, *43*, 3012–3022. [CrossRef]
5. Wang, Y.; Liu, B.Y.; Li, L.; Li, Q.; Zhou, S.B. Research progress on the microstructure, mechanical and structural properties of geopolymer concrete. *Chem. New Mater.* **2026**, 1–10. [CrossRef]
6. Yuan, J.; Du, H.Z. Research on waste tire recycling under extended producer responsibility system (EPR). *Renew. Resour. Circ. Econ.* **2020**, *13*, 22–24.
7. Yao, W.J.; Liu, Y.S.; Wang, T.Y.; Pang, J.Y. Performance degradation and microstructure of rubber/concrete after salt freeze-thaw cycles. *J. Compos. Sci. Technol.* **2021**, *38*, 4294–4304.
8. Xue, G.; Zhu, H.J.; Xu, S.; Liu, L.Q. Uniaxial compression fatigue performance of rubber concrete. *Eng. Mech.* **2022**, *39*, 203–211.
9. Jin, L.; Ye, Y.; Sun, H.Q. Dynamic response of rockfall impact crushed stone-rubber mixed cushion. *J. Vib. Shock* **2026**, *45*, 244–254. [CrossRef]
10. Shi, Z.Y.; Yang, J.; Hu, Y.H.; Yang, F.Y.; Li, Z.G.; Li, H.B. Basic performance prediction of rubber asphalt based on GA-II BP neural network. *Sci. Technol. Eng.* **2025**, *25*, 15294–15301.
11. Li, D.; Wang, Z.Q.; Jin, L.; Du, X.L. Experimental study on the effect of specimen size and loading strain rate on the splitting tensile strength of steel fiber recycled concrete. *J. Compos. Sci. Technol.* **2026**, *43*, 2973–2983. [CrossRef]
12. Fadiel, A.A.M.; Mohammed, N.S.; Abu-Lebdeh, T.; Munteanu, I.S.; Niculae, E.; Petrescu, F.I.T. A Comprehensive Evaluation of the Mechanical Properties of Rubberized Concrete. *J. Compos. Sci.* **2023**, *7*, 129. [CrossRef]
13. He, S.; Zhong, H.; Chen, Z.; Chen, H.; Chen, J.; Yu, Z. Effects of Thermal Cycles on Mechanical Properties of RPECC: Static and Dynamic Splitting Tensile Performance. *Materials* **2025**, *18*, 994. [CrossRef] [PubMed]
14. Cocchiara, M.C.; Prieto, M.I.; Cobo, A.; Olmedo, F.I. Influence of FRP Confinement on the Compressive Strength of Concrete with Recycled Rubber. *Fibers* **2026**, *14*, 51. [CrossRef]
15. Wen, J.; Xiong, Z.; Wu, X.; Li, X.; Luo, W. Enhanced Dynamic Compressive Behavior of Rubberized Concrete with Steel–Glass Fibers. *Buildings* **2026**, *16*, 472. [CrossRef]
16. Luo, C.; Wang, H.; Cai, D.; Wang, A.; Zhang, L.; Wang, D.; Wang, C.; Kong, D.; Huang, S.; Xu, C. Synergistic Effects of Steel Fiber and Rubber Powder on the Physico-Mechanical Properties of UHPC. *Sustainability* **2026**, *18*, 846. [CrossRef]
17. Tarekegn, Y.G.; Lahmer, T.; Tarekegn, A.G.; Ftwi, E.G. Three-Dimensional Simulation on the Influence of Coated Rubber Chips on Concrete Properties. *Buildings* **2025**, *15*, 4186. [CrossRef]
18. Qureshi, M.; Li, J.; Wu, C.; Sheng, D. Mechanical strength of rubberized concrete: Effects of rubber particle size, content, and waste fiber reinforcement. *Constr. Build. Mater.* **2024**, *444*, 137868. [CrossRef]
19. Xue, G.; Dong, Y.J.; Yi, X.; Gao, P. Experimental study on fracture toughness of rubber concrete. *Build. Struct.* **2022**, *52*, 115–119+126.
20. Hu, Y.L.; Gao, P.W.; Li, F.R.; Ma, A.Q.; Yu, Z.P. Experimental study on mechanical properties of rubber concrete with different replacement rates. *J. Build. Mater.* **2020**, *23*, 85–92.
21. El-Zohairy, A.; Sanchez, M.; Abediniangerabi, B.; Moler, P. Performance of Rubberized Concrete and the Effect of Temperature and Stainless Steel Fibers. *Buildings* **2023**, *13*, 280. [CrossRef]
22. Dong, S.; Shi, F.W.; Li, P.; Zhao, Q.X. Working performance and mechanical properties of steel fiber rubber concrete. *J. Compos. Sci. Technol.* **2025**, *42*, 430–440. [CrossRef]
23. Zhao, Q.H.; Dong, S.; Zhu, H. Experimental study and constitutive model of uniaxial compression full curve of steel fiber-rubber/concrete. *J. Compos. Sci. Technol.* **2021**, *38*, 2359–2369. [CrossRef]
24. Peng, K.; Zhou, J.Z.; Wu, W.X. Effect of steel fiber content on mechanical properties of rubber concrete. *J. Hubei Univ. Technol.* **2019**, *34*, 118–120.
25. Wang, J.J.; Zha, W.H.; Peng, Q.F. Experimental study on mechanical properties of concrete under loading and unloading conditions. *Saf. Coal Mines* **2020**, *51*, 44–49. [CrossRef]
26. Zhao, H.R. Study on Mechanical and Durability Performance of Straw Ash-Rubber Concrete. Master's Thesis, Liaoning University of Technology, Jinzhou, China, 2023. [CrossRef]
27. Yan, J.; Gao, Y.; Tang, M.; Ding, N.; Xu, Q.; Peng, M.; Zhao, H. Experimental Study on the Mechanical Properties of Recycled Spiral Steel Fiber-Reinforced Rubber Concrete. *Buildings* **2024**, *14*, 897. [CrossRef]

28. Kroviakov, S.; Kryzhanovskyi, V.; Hedulian, D. Comparison of the Corrosion Resistance of Fiber-Reinforced Concrete with Steel and Polypropylene Fibers in an Acidic Environment. *Constr. Mater.* **2025**, *5*, 6. [CrossRef]
29. Shen, K.; Liu, J.P.; Rao, Q.H.; Liu, Z.L.; Jin, S.B.; Liu, P. Modified statistical constitutive model for tensile-shear damage of sandstone and concrete materials based on acoustic emission clustering under thermo-mechanical coupling. *Trans. Nonferrous Met. Soc. China* **2026**, *36*, 2424–2442.
30. Su, J.; Liu, J.X.; Liu, N.; Wu, L.; Wang, Y.J.; Li, X.Q.; Zhang, Y. Cluster analysis on tensile damage behavior of 3DN C/SiC composites using acoustic emission. *Acta Mater. Compos. Sin.* **2026**, 1–20. [CrossRef]
31. Chen, Z.B.; Fang, Y.F.; Huang, W.; Lai, H.; Cao, G. Microstructure evolution of granite residual soil during shearing based on SEM and NMR. *J. Eng. Geol.* **2026**, *34*, 890–900. [CrossRef]
32. *GB 175-2023*; Common Portland Cement. State Administration for Market Regulation and Standardization Administration of China: Beijing, China, 2023.
33. *GB/T 8076-2025*; Concrete Admixtures. State Administration for Market Regulation and Standardization Administration of China: Beijing, China, 2025.
34. *JGJ 55-2011*; Specification for Mix Proportion Design of Ordinary Concrete. Ministry of Housing and Urban-Rural Development of the People's Republic of China: Beijing, China, 2011.
35. *GB/T 50081-2019*; Standard for Test Methods of Mechanical Properties of Concrete. Ministry of Housing and Urban-Rural Development of the People's Republic of China: Beijing, China, 2019.
36. *ASTM C496/C496M-17*; Standard Test Method for Splitting Tensile Strength of Cylindrical Concrete Specimens. ASTM International: West Conshohocken, PA, USA, 2017.
37. Li, M.; Gao, Y.; Wang, C.; Li, Y.; Fan, T. Impact Resistance Test and Numerical Simulation Study of Scrap Steel Fiber Rubber Concrete. *Buildings* **2025**, *15*, 2857. [CrossRef]
38. Jiang, Z.; Zhu, Z.; Accornero, F. Tensile-to-Shear Crack Transition in the Compression Failure of Steel-Fiber-Reinforced Concrete: Insights from Acoustic Emission Monitoring. *Buildings* **2024**, *14*, 2039. [CrossRef]

Disclaimer/Publisher's Note: The statements, opinions and data contained in all publications are solely those of the individual author(s) and contributor(s) and not of MDPI and/or the editor(s). MDPI and/or the editor(s) disclaim responsibility for any injury to people or property resulting from any ideas, methods, instructions or products referred to in the content.